

# Differential Unfolding: Efficient Unfolding Reconstruction for Video Snapshot Compressive Imaging

Muyuan Zhang<sup>1,\*</sup>, Jiancheng Zhang<sup>1,\*</sup>, Haijin Zeng<sup>2</sup>, and Yin-ping Zhao<sup>1,†</sup>

<sup>1</sup> Northwestern Polytechnical University, Xi'an, China

<sup>2</sup> Harbin Institute of Technology (Shenzhen), Shenzhen, China

**Abstract.** While Deep Unfolding Networks (DUNs) dominate video Snapshot Compressive Imaging (SCI), they remain constrained by a uniform design philosophy. Existing methods repeatedly stack high-complexity priors with identical structures, ignoring the fact that optimization trajectories converge toward static states. This results in representation stagnation, where high-cost computations are wasted on minimal feature updates. To address this inefficiency, we present Differential Unfolding (DU), a heterogeneous framework that replaces uniform repetition with dynamic evolution. Central to DU is the Differential Evolutionary Framework (DEF), which partitions the unfolding process into two complementary roles: structural anchoring and differential evolution. In this scheme, high-parameter general stages are sparsely deployed to generate high-fidelity feature foundations. Complementing these, lightweight differential stages employ a Differential Representation Prior (DRP) to propagate and refine these foundational features through a differential mechanism. By integrating Differential Representation Attention (DRA) for evolving attention maps and a Differential Modulated FFN (DM-FFN) for feature rectification, DRP effectively models cross-stage variations with minimal overhead. By focusing computational resources on dynamic evolution rather than static redundancy, DU achieves a superior trade-off between accuracy and efficiency. Extensive experiments verify that our method establishes new state-of-the-art results while significantly slashing computational overhead. <https://github.com/Muyuan-Zhang/DU>

**Keywords:** Snapshot compressive imaging · Video reconstruction · Deep Unfolding

## 1 Introduction

Video Snapshot Compressive Imaging (SCI) [12, 13, 16, 23, 24, 39], rooted in the principles of Compressive Sensing (CS) [10], has revolutionized high-speed video acquisition. This technique ingeniously encodes a sequence of high-speed video

---

\* Equal Contribution, † Corresponding Author.

frames into a single 2D measurement, enabling capture with a conventional low-speed camera. However, the subsequent recovery of the original video constitutes a severely ill-posed inverse problem. A spectrum of solutions has been proposed to tackle this challenge, ranging from traditional model-based [15, 35, 36, 38] and plug-and-play [40, 41] methods to modern end-to-end learning approaches [4, 5, 7, 8, 18, 22, 25–29]. Among these, deep unfolding methods [19, 20, 31–34, 37, 42] have emerged as a particularly promising direction. By embedding deep unfolding networks (DUNs) within iterative optimization algorithms, these methods elegantly integrate the principled structure of classical algorithms with the powerful learning capacity of deep.

Despite their success, most existing deep unfolding networks (DUNs) suffer from a pervasive structural limitation: they adopt a homogeneous stage design, where prior networks with identical architectures and comparable capacity are redundantly applied across all unfolding iterations. While this design preserves interpretability and maintains a rigorous correspondence to iterative optimization, it overlooks an intrinsic dynamic nature of the reconstruction trajectory. As the unfolding proceeds, the reconstruction typically approaches convergence, causing intermediate feature states to become increasingly stagnant. Nevertheless, conventional prior modules continue to execute exhaustive mappings at every stage, irrespective of the diminishing magnitude of state updates. This architectural mismatch between saturating representation evolution and static model culminates in a phenomenon we term Inter-Stage Representation Homogeneity, which inevitably introduces significant computational redundancy. Our empirical observations confirm this effect. As illustrated in Fig. 2, feature heatmaps from consecutive stages exhibit striking similarity, indicating that the representation evolution across stages is limited. Cosine similarity between stage-wise features remains consistently high, suggesting that successive updates introduce only marginal perturbations. In such scenarios, repeated application of a full prior network does not substantially alter the representation but instead reinforces pre-established structures. As the incremental information decreases, the network continues to execute computationally intensive transformations on highly similar feature states, resulting in substantial redundancy. Consequently, the unfolding process becomes progressively inefficient in later stages, where disproportionate computational resources are squandered on minimal representational refinements. This observation exposes a fundamental structural deficiency in existing DUNs: the lack of a differentiation mechanism that distinguishes between comprehensive representation reconstruction and incremental evolution.

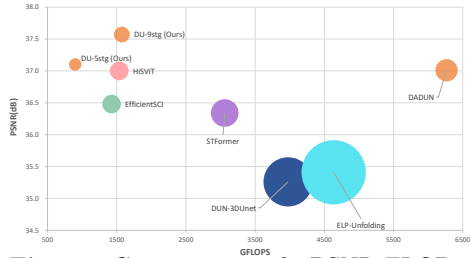


**Fig. 1:** Comparison of PSNR-FLOPs-Params on 6 grayscale datasets of the proposed DU and competing methods. The radius indicates the number of parameters.

To address the inefficiency stemming caused by inter-stage representation homogeneity, we propose Differential Unfolding (DU), a novel paradigm for efficient video SCI reconstruction. Unlike conventional unfolding designs that repeatedly apply identical priors throughout the optimization trajectory, DU introduces structural adaptability into the unfolding process by explicitly modeling how representations evolve during convergence. The proposed framework is built upon two key components: the Differential Evolutionary Framework (DEF) and the Differential Representation Prior (DRP). Departing from homogeneous architectures, DEF partitions the reconstruction trajectory into periodic general unfolding stages and differential evolutionary stages. General stages employ a high-parameter spatial-temporal backbone for holistic restructuring, while differential stages focus on incremental updates as inter-stage variations become increasingly subtle. This periodic alternation is motivated by the non-uniform dynamics of iterative reconstruction. By reintroducing general unfolding, DEF prevents error accumulation and representation drift, while intermediate refinement stages circumvent redundant computation on nearly converged states. To efficiently model incremental evolution, the DRP captures cross-stage variations rather than reconstructing features from scratch. It consists of Differential Representation Attention (DRA), which tracks evolving attention dependencies, and a Differential Modulated Feed-Forward Network (DM-FFN), which adaptively modulates features via differential-driven gating. This stage-wise design mitigates redundant computation induced by representation homogeneity while preserving essential structural updates, leading to improved efficiency and enhanced modeling of dynamic regions and fine details.

Our main contributions are summarized as follows:

- We identify and systematically analyze inter-stage representation homogeneity in deep unfolding networks, revealing it as a fundamental source of computational redundancy during iterative reconstruction.
- We propose the Differential Unfolding (DU) method with a Differential Evolutionary Framework (DEF), which introduces a periodic unfolding mechanism that dynamically alternates between general unfolding and differential evolutionary stages.
- We design a Differential Representation Prior (DRP) that explicitly models cross-stage representation evolution, enabling efficient refinement under highly similar feature states and reducing unnecessary computation.
- Extensive experiments demonstrate that DU achieves state-of-the-art reconstruction performance while significantly reducing parameter count and computational complexity across multiple SCI benchmarks.

## 2 Related Work

### 2.1 Video SCI Reconstruction

Traditional model-based algorithms [15, 38], while possessing rigorous mathematical interpretability, have gradually been abandoned due to their long solving

times and low reconstruction quality. With the advancement of deep learning, deep neural networks have become a research hotspot due to their faster reconstruction speed and higher reconstruction quality. For example, BIRNAT [8] utilizes bidirectional recurrent neural networks for reconstruction. STFormer [26] employs both temporal and spatial transformers to account for temporal and spatial degradations separately. EfficientSCI [25] combines the local modeling capabilities of convolutional networks with the long-range modeling capabilities of transformers, using dense connections to reduce the computational cost of the model. HiSViT [28] takes into account the imaging characteristics of video SCI systems and focuses on spatial restoration in the early stages of the model.

## 2.2 Deep Unfolding Methods

Previous model-based methods typically require manually designed priors and lack flexibility when handling different reconstruction scenarios. The deep unfolding method [19, 20, 31, 32, 34, 42] combines traditional mathematical iterative algorithms with deep neural networks, retaining both mathematical interpretability and the ability to adaptively adjust the priors. ADMM-Net [19] is the first to propose a deep unfolding framework for video SCI reconstruction. ELP-Unfolding [34] leverages ensemble priors to achieve both high reconstruction speed and accuracy within a single network. DUN-3DUnet [31] considers information loss between stages and uses DFMA to fuse information across stages. CTM-SCI [42] introduces uncertainty estimation to investigate the high-frequency information. DADUN [37] introduces a degradation-aware deep unfolding framework that uses estimated priors and a BiP-CRNN to guide iterative reconstruction of video SCI sequences. However, for Video SCI tasks involving coupled spatial and temporal degradations, existing unfolding methods often produce highly similar feature representations across consecutive stages. Such stage-wise homogenization limits effective representation evolution, leading to redundant computations and restricting the model’s ability to progressively refine dynamic scene details.

## 3 Proposed Method

### 3.1 Mathematical Model of Video SCI

In the video SCI system, three-dimensional high-speed video frames are modulated by multiple masks, then integrated along the temporal dimension, and finally captured by a two-dimensional camera sensor as compressed two-dimensional measurements. Fig. 2 illustrates the compression process of video SCI. Mathematically, high-speed grayscale video frames  $F \in \mathbb{R}^{H \times W \times T}$  are modulated by masks with patterns  $M \in \mathbb{R}^{H \times W \times T}$ . After temporal compression, the two-dimensional compressed measurement  $G \in \mathbb{R}^{H \times W}$  is captured by the camera sensor. This process can be expressed as:

$$G(h, w) = \sum_{i=1}^T M(h, w, i) \odot F(h, w, i) + N, \quad (1)$$

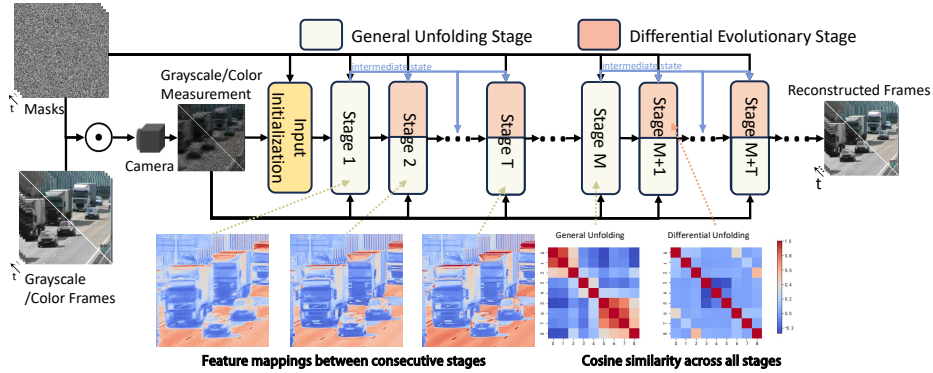


**Fig. 2:** The compression process of VideoSCI and the reconstruction process of the unfolding framework. We present feature maps from some stages of the general unfolding, along with the cosine similarities between the stages of general unfolding and differential unfolding.

where  $\odot$  denotes the element-wise multiplication (Hadamard product),  $h$  and  $w$  represent spatial coordinates, and  $N \in \mathbb{R}^{H \times W}$  represents noise introduced during the imaging process. Please note that, for the sake of simplicity, we have omitted the color channels. The matrix-vector form of Eq. (1) can be written as:

$$g = \Phi f + n, \quad (2)$$

where  $g = \text{vex}(G) \in \mathbb{R}^{HW}$ ,  $f = \text{vex}(F) \in \mathbb{R}^{HWT}$ , and  $n = \text{vex}(N) \in \mathbb{R}^{HW}$  denote the vectorized forms of the measurement  $G$ , the original video frames  $F$ , and the noise  $N$ , respectively.

### 3.2 General Unfolding Methods

Traditional deep unfolding algorithms build the unfolding framework by solving the following subproblem:

$$\hat{f} = \underset{f}{\operatorname{argmin}} \frac{1}{2} \|g - \Phi f\|^2 + \tau R(f), \quad (3)$$

where  $\frac{1}{2} \|g - \Phi f\|^2$  is the data fidelity term,  $R(f)$  is the image prior term, and  $\tau$  is the hyperparameter that balances their importance. For example, in the case of the HQS method, the problem is then decomposed into two alternating steps: a gradient descent step and a prior mapping step, which are solved iteratively as follows:

$$z_k = f_{k-1} + \rho \Phi^T [(g - \Phi z_{k-1}) / (\Phi \Phi^T)], \quad (4)$$

$$f_k = \mathcal{P}_k(z_k), \quad (5)$$

where  $k$  represents the iteration stage,  $\rho$  is the step size for the iteration is the step size for the iteration, which can be estimated by a simple network from [3],

and  $\mathcal{P}$  denotes the prior mapping module. Fig. 2 depicts the architecture of the general unfolding framework. We follow previous works [8, 25, 31] and use a similar input initialization module to obtain a good initial input  $f_0$ . While this formulation is effective, it relies on a homogeneous structure, where the same prior network architecture is used across all stages of the unfolding process. This leads to a phenomenon we call inter-stage representation homogeneity, where successive stages become increasingly similar, causing computational redundancy and inefficiencies. To address this issue, we introduce the Differential Evolutionary Framework (DEF), which adapts the unfolding process by introducing periodic general unfolding and differential evolutionary stages.

### 3.3 Differential Evolutionary Framework

This section presents the core concept of DU, introducing how DEF performs incremental updates across stages and how the different unfolding stages are periodically organized. Starting from the general unfolding framework, we decompose the prior mapping module  $\mathcal{P}_k$  in Eq.(5) into an encoder  $\mathcal{E}_k$  and a decoder  $\mathcal{D}_k$ , and obtain the intermediate state  $s$  as the reference feature. This can be mathematically represented as:

$$s_k = \mathcal{E}_k(z_k), \quad (6)$$

$$f_k = \mathcal{D}_k(s_k). \quad (7)$$

The intermediate state  $s_k$  contains rich feature representations accumulated during the  $k$ -th unfolding iteration stage, which is then used in the next stage for refinement modeling reference, enabling the update of redundant components while simultaneously generating a new reference intermediate state  $s_{k+1}$ . By repeatedly leveraging intermediate state features to update redundant information while preserving effective features, homogeneous representation modeling is effectively mitigated, and the capture of dynamic regions and fine details is enhanced. To balance the recovery of primary features with the update of redundant information, the unfolding stages are divided into general unfolding stages, responsible for primary feature reconstruction, and differential evolutionary stages, responsible for refinement updates. Mathematically, the unfolding process can be described as follows:

$$f_{k+1} = \begin{cases} \mathcal{P}_{k+1}^{\text{heavy}}(z_{k+1}), & \text{General Unfolding Stage,} \\ \mathcal{P}_{k+1}^{\text{diff}}(z_{k+1}, s_k), & \text{Differential Evolutionary Stage.} \end{cases} \quad (8)$$

where  $\mathcal{P}_{k+1}^{\text{heavy}}$  represents a high-parameter prior module designed to drastically model the feature representation, and  $\mathcal{P}_{k+1}^{\text{diff}}$  represents a lightweight differential refinement operation designed to capture the differences between consecutive stages as shown in Fig. 3.

By periodically introducing general unfolding stages, the model can continuously generate a high-fidelity feature foundation and progressively refine redundant components in subsequent stages, achieving stage-wise dynamic reconstruction. Through this mechanism, the DEF not only avoids the computational

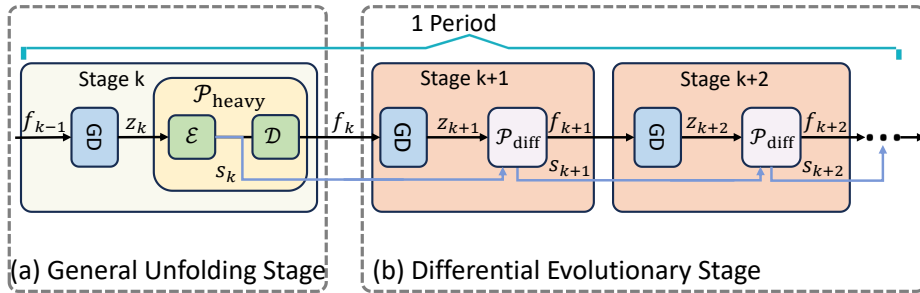


**Fig. 3:** Illustration of the Differential Evolutionary Framework (DEF). Our DEF starts from the general unfolding stages within one period, where the intermediate states are subsequently utilized in the next differential evolutionary stage for adaptive feature update. (a) The general unfolding stages. (b) The differential evolutionary stages.

redundancy of repeatedly applying high-capacity operations but also allows for more efficient and targeted updates, leading to improved model performance and faster convergence. To implement  $\mathcal{P}^{\text{diff}}$  in the evolutionary refinement stage in a computationally efficient manner, we introduce the Differential Representation Prior (DRP). DRP is designed to capture the differential variations between consecutive stages, ensuring that only meaningful updates are applied during each refinement step and that redundant computations are minimized. In the next section, we describe the architecture and operation of the DRP in detail.

### 3.4 Differential Representation Prior

In this section, we provide a detailed description of how our DRP achieves feature refinement across stages. The DRP consists of two core components: Differential Representation (DRA), which effectively updates features by computing the differences between the attention maps of the current feature representation and the intermediate state from the previous stage; and Differential Modulated Feed-Forward Network (DM-FFN), which modulates the spatial-temporal enhanced features by generating modulation parameters through a difference-driven convolutional module.

**Network Architecture.** As demonstrated in Fig. 4 (a), DRP contains two cascaded spatial-temporal factorized transformer layers [1, 2], employs DRA to update information in spatial and temporal domains, respectively. Following DRA, the proposed DM-FFN leverages the intermediate state to generate modulation information for feature rectification. Four Layer Normalizations (LN) are employed to stabilize training and enhance generalization ability.

**Differential Representation Attention.** DRA captures the evolving relationships between consecutive stages through attention mechanisms. It computes

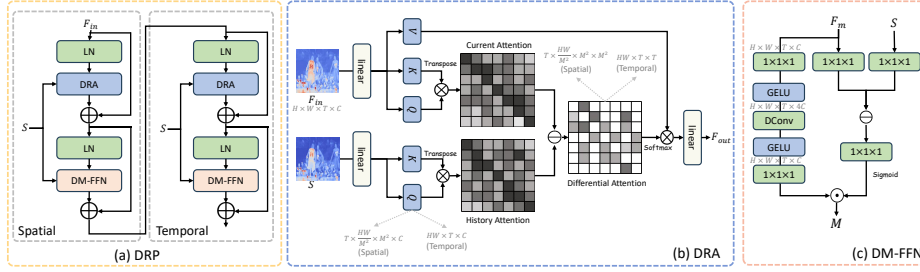


**Fig. 4:** (a) The backbone structure of DRP. (b) and (c) are details of DRA and DM-FFN.

differential attention by comparing the current feature representation with the intermediate state from the previous stage. The core idea behind DRA is that attention scores corresponding to similar regions are attenuated, while those exhibiting greater discrepancies between stages are amplified. This attention mechanism highlights the regions where there is the most change, allowing the model to focus on the evolving aspects of the reconstruction while minimizing redundant information.

As illustrated in Fig. 4 (b), the input feature  $F_{in} \in \mathbb{R}^{H \times W \times T \times C}$  embedded by an implicit position [9] is linearly projected into the query  $Q_{in} \in \mathbb{R}^{H \times W \times T \times C}$ , key  $K_{in} \in \mathbb{R}^{H \times W \times T \times C}$  and value  $V_{in} \in \mathbb{R}^{H \times W \times T \times C}$  as:

$$Q_{in} = F_{in}W_{Q_{in}}, K = F_{in}W_{K_{in}}, V = F_{in}W_{V_{in}}, \quad (9)$$

where  $W_{Q_{in}} \in \mathbb{R}^{C \times C}$ ,  $W_{K_{in}} \in \mathbb{R}^{C \times C}$  and  $W_{V_{in}} \in \mathbb{R}^{C \times C}$  are learnable parameters. The intermediate state  $S \in \mathbb{R}^{H \times W \times T \times C}$  is linearly projected into query  $Q_r \in \mathbb{R}^{H \times W \times T \times C}$  and key  $K_r \in \mathbb{R}^{H \times W \times T \times C}$  as:

$$Q_r = SW_{Q_r}, K_r = SW_{K_r} \quad (10)$$

where  $W_{Q_r} \in \mathbb{R}^{C \times C}$  and  $W_{K_r} \in \mathbb{R}^{C \times C}$  are learnable parameters. For the spatial domain,  $Q_{in}, K_{in}, V_{in}, Q_r, V_r$  are partitioned into non-overlapping windows of  $M \times M$  tokens and reshaped into  $\mathbb{R}^{T \times \frac{HW}{M^2} \times M^2 \times C}$ ; for the temporal domain,  $Q_{in}, K_{in}, V_{in}, Q_r, V_r$  are reshaped into  $\mathbb{R}^{HW \times T \times C}$ .  $Q_{in}, K_{in}, V_{in}, Q_r, V_r$  are subsequently split along the channel dimension into  $N$  attention heads. The dimension of each head is  $d = \frac{C}{N}$ . The illustration in Fig. 4 (b) depicts the situation where  $h = 1$  and some details are omitted for simplification. The similarity matrix for each head for  $F_{in} \in \mathbb{R}^{H \times W \times T \times C}$  and  $S \in \mathbb{R}^{H \times W \times T \times C}$  are computed as:

$$\begin{aligned} M_{in} &= Q_{in}K_{in}^T, \\ M_r &= Q_rK_r^T. \end{aligned} \quad (11)$$

The spatial similarity matrix is given by  $M_{in}, M_r \in \mathbb{R}^{T \times \frac{HW}{M^2} \times M^2 \times M^2}$ , and the temporal similarity matrix is given by  $M_{in}, M_r \in \mathbb{R}^{HW \times T \times T}$ . By computing

the difference between two similarity matrices, we can obtain a more efficient attention matrix, denoted as:

$$M = M_{in} - M_r. \quad (12)$$

The final attention  $Atten_i$  is calculated inside each head as:

$$Atten_i = \text{softmax}(M_i/\sqrt{d_h})V_i \quad (13)$$

Finally, the outputs of all  $N$  attention heads are concatenated along the channel dimension, reshaped, and then processed through a linear projection as:

$$F_{out} = \text{Concat}_i^N((Atten_i)V_i)W + b, i = 1, \dots, h, \quad (14)$$

**Differential Modulated Feed-Forward Network.** To maximize the use of intermediate features, preserving useful information while discarding redundant data, we designed the DM-FFN. DM-FFN performs pixel-level modulation on the redundant information present in the current features through feature modulation. As shown in Fig. 4 (c), DM-FFN contains two branches: a feature branch, which models local spatiotemporal information, and a modulation branch, which generates weights by leveraging both the current features and the intermediate state to modulate the enhanced features. In the feature branch, for the input  $F_m$ , we first use a  $1 \times 1 \times 1$  convolution to expand the channels fourfold, then apply a depth-wise convolution DConv to extract local spatiotemporal information—with a kernel size of  $1 \times 3 \times 3$  in the spatial domain and  $3 \times 1 \times 1$  in the temporal domain—followed by a  $1 \times 1 \times 1$  convolution to reduce the dimensionality and obtain the enhanced feature representation  $F_e$ . In the modulation branch, we first map the current features and the intermediate state using a  $1 \times 1 \times 1$  convolution and compute their difference. This is then passed through a sigmoid function to obtain pixel-level weights, which are multiplied by the enhanced features  $F_e$  to produce the modulated output  $F_{out}$ . Mathematically, the process can be expressed as:

$$F_e = \text{ConvLayer}(F_m), \quad (15)$$

$$w = \text{Sigmoid}(\text{Conv}_1(\text{Conv}_1(F_m) - \text{Conv}_1(S))), \quad (16)$$

$$F_{out} = F_e \odot w, \quad (17)$$

where ConvLayer denotes the convolutional layer in the feature branch, Conv<sub>1</sub> denotes the  $1 \times 1 \times 1$  convolution in the modulation branch, and  $w$  represents the pixel-level weights obtained from the modulation branch.

## 4 Experiment

### 4.1 Implementation Details

**Model Setting.** We provide two model settings: DU-5stg and DU-9stg to balance parameters and performance of the proposed network. The channel number of DRP is set to 48, and the window size of DRA is set to  $8 \times 8$ . The periodicity of DEF is set to 4.

**Table 1:** Quantitative results of different methods on grayscale videos in terms of PSNR (dB)  $\uparrow$ , SSIM  $\uparrow$ , Params (M)  $\downarrow$ , and FLOPs (G)  $\downarrow$ . The best and second-best results are highlighted in bold and underlined, respectively.

| Method             | Params      | FLOPs          | Kobe                        | Traffic                     | Runner                      | Drop                        | Crash                       | Aerial                      | Average                     |
|--------------------|-------------|----------------|-----------------------------|-----------------------------|-----------------------------|-----------------------------|-----------------------------|-----------------------------|-----------------------------|
| GAP-TV [38]        | -           | -              | 26.46, 0.885                | 20.89, 0.715                | 28.52, 0.909                | 34.63, 0.970                | 24.82, 0.838                | 25.05, 0.828                | 26.73, 0.858                |
| DeSCI [15]         | -           | -              | 33.25, 0.952                | 28.71, 0.925                | 38.48, 0.969                | 43.10, 0.993                | 27.04, 0.909                | 25.33, 0.860                | 32.65, 0.935                |
| PnP-PFDNet [40]    | -           | -              | 30.50, 0.926                | 24.18, 0.828                | 32.15, 0.933                | 40.70, 0.989                | 25.42, 0.849                | 25.27, 0.829                | 29.70, 0.892                |
| PnP-FastDVNet [41] | -           | -              | 32.73, 0.947                | 27.95, 0.932                | 36.29, 0.962                | 41.82, 0.989                | 27.32, 0.925                | 27.98, 0.897                | 32.35, 0.942                |
| DUN-3DUNet [31]    | 61.91       | 3975.83        | 35.00, 0.969                | 31.76, 0.966                | 40.03, 0.980                | 44.96, <b>0.995</b>         | 29.33, 0.956                | 30.46, 0.943                | 35.26, 0.968                |
| ELP-Unfolding [34] | 565.73      | 4634.94        | 34.41, 0.966                | 31.58, 0.962                | 41.16, 0.986                | 44.99, <b>0.995</b>         | 29.65, 0.959                | 30.68, 0.944                | 35.41, 0.969                |
| STFormer [26]      | 19.48       | 3060.75        | 35.53, 0.973                | 32.15, 0.967                | 42.64, 0.988                | 45.08, <b>0.995</b>         | 31.06, 0.970                | 31.56, 0.953                | 36.34, 0.974                |
| EfficientSCI [25]  | 8.82        | 1426.38        | 35.76, 0.974                | 32.30, 0.968                | 43.05, 0.988                | 45.18, <b>0.995</b>         | 31.13, 0.971                | 31.50, 0.953                | 36.48, 0.975                |
| DUN-3DUNet++ [6]   | 8.08        | <u>1063.01</u> | 35.70, 0.974                | 32.24, 0.968                | 42.73, 0.988                | 45.33, <b>0.995</b>         | 31.02, 0.971                | 31.64, 0.953                | 36.44, 0.975                |
| HiSViT [28]        | 8.98        | 1535.92        | <u>36.24</u> , <u>0.976</u> | 33.06, <u>0.973</u>         | 43.84, <b>0.991</b>         | 45.55, <b>0.995</b>         | 31.62, <u>0.976</u>         | 31.67, <u>0.957</u>         | 37.00, <u>0.978</u>         |
| DADUN [37]         | 12.67       | 6266.15        | 36.23, <u>0.976</u>         | <u>33.08</u> , 0.972        | 43.60, 0.990                | 45.49, <b>0.995</b>         | <u>31.93</u> , <u>0.976</u> | 32.00, 0.958                | 37.01, <u>0.978</u>         |
| DU-5stg (Ours)     | <b>3.95</b> | <b>899.64</b>  | 36.11, <u>0.976</u>         | 32.80, 0.971                | <u>43.86</u> , 0.990        | <u>45.84</u> , <b>0.995</b> | 31.79, 0.975                | <u>32.18</u> , <u>0.959</u> | 37.10, <u>0.978</u>         |
| DU-9stg (Ours)     | <u>6.36</u> | 1574.37        | <b>36.51</b> , <b>0.978</b> | <b>33.45</b> , <b>0.974</b> | <b>44.75</b> , <b>0.991</b> | <b>45.99</b> , <b>0.995</b> | <b>32.47</b> , <b>0.978</b> | <b>32.27</b> , <b>0.961</b> | <b>37.57</b> , <b>0.980</b> |

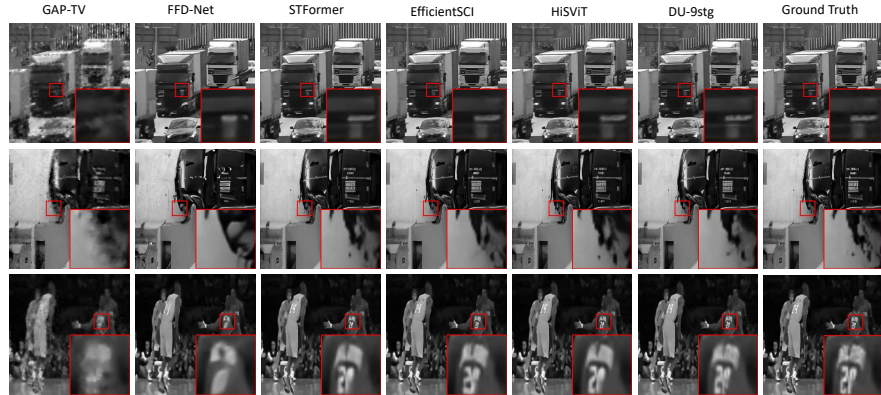


**Fig. 5:** Visual results of competitive methods on grayscale video frames.

**Experiment Setting.** The proposed method is implemented using PyTorch and trained on a single RTX PRO 6000 GPU. Following previous works, our models are trained in the DAVIS2017 dataset [21] with the same data augmentation in [25]. To verify model performance, we conduct experiments on six grayscale/color benchmark videos with a resolution of  $8 \times 256 \times 256/8 \times 512 \times 512 \times 3$  pixels and on real captured grayscale videos (Duonimo and WaterBallon [22]) with the resolution of  $10 \times 512 \times 512$  pixels. We adopt the Adam optimizer [14] with settings  $\beta_1 = 0.9$  and  $\beta_2 = 0.999$ , and the initial learning rate is set to  $4 \times 10^{-4}$  and adopt the Cosine Annealing learning rate scheme [17] to implement end-to-end training. After training for over 100 epochs on the pixels of  $8 \times 128 \times 128(\times 3)$ , we continued training for over 30 epochs on the pixels of  $8 \times 256 \times 256(\times 3)$ . The Peak Signal to Noise Ratio (PSNR) and Structural Similarity Index Metric (SSIM) [30] are used as performance metrics to evaluate the reconstruction quality. We choose the root mean square error (RMSE) as the loss function. To encourage each stage in the unfolding framework to contribute effectively to the final reconstruction, we design a full-stage loss function,

where the weight of each stage is controlled by an exponential function. The loss function can be defined as:

$$L = \frac{1}{N} \sum_{i=1}^N \sum_{m=1}^M \|e^{\beta m} \bar{X}_m^i - X\|_2^2, \quad (18)$$

where  $N$  denotes the number of training samples,  $M$  represents the total number of stages of the model,  $e$  is the base of the natural logarithm, and  $\beta$  is a hyperparameter used to control the weighting across different stages. More model details and additional results are in the supplementary material.

## 4.2 Results on Grayscale Simulation Videos

We selected previous state-of-the-art (SOTA) models for comparison, including model-based methods (GAP-TV [20], DeSCI [15]), plug-and-play methods (PnP-FFDNet [40], PnP-FastDVDnet [41]), Transformer-based methods (STFormer [26], EfficientSCI [25], EfficientSCI++ [6], HiSViT [28]) and deep unfolding methods (DUN-3DUNet [31], ELP-Unfolding [34], DADUN [37]) on 6 simulated grayscale datasets. To intuitively show the effectiveness of our DU, we provide Performance-FLOPs-Params comparisons of SOTA methods in Fig. 1. Tab. 1 presents the detailed quantitative comparison results of our method with other methods in terms of PSNR, SSIM, parameters, and FLOPs. It can be observed that the proposed DU-5stg outperforms other methods, with the least FLOPs and parameters. Compared with the previous method with the lowest parameter count and computational cost, EfficientSCI++, our method achieves an improvement of over 0.6 dB. Compared to the previous best deep unfolding method DADUN, our DU-9stg only requires 50.2% of the parameters and 25.12% of the FLOPs while achieving an improvement of 0.56 dB. Fig. 5 presents a visual comparison between DU and several other methods. By magnifying certain local regions, our DU demonstrates the ability to reconstruct sharper edges and finer details.

## 4.3 Results on Color Simulation Videos

For color simulation videos, we selected previous state-of-the-art (SOTA) models for comparison, including model-based methods (GAP-TV [38], DeSCI [15]), plug-and-play methods (PnP-FFDNet [40], PnP-FastDVDNet [41]), RNN-based method BIRNAT [8] Transformer-based methods (STFormer [26], EfficientSCI [25], EfficientSCI++ [6], HiSViT [28]), and deep unfolding method DADUN [37] for comparison. Tab. 2 presents the detailed quantitative comparison results of our method with other methods in terms of PSNR, SSIM, parameters, and FLOPs. Compared with previous Transformer-based methods HiSViT, our approach achieves higher performance while requiring fewer parameters and comparable cost. Fig. 6 presents a visual comparison between DU and several other methods. By magnifying certain local regions, our DU demonstrates the ability to reconstruct sharper edges and finer details.

**Table 2:** Quantitative results of different methods on color videos in terms of PSNR (dB)  $\uparrow$ , SSIM  $\uparrow$ , Params (M)  $\downarrow$ , and FLOPs (G)  $\downarrow$ . The best and second-best results are highlighted in bold and underlined, respectively.

| Method              | Params      | FLOPs          | Beauty              | Bosphorus           | Jockey              | Runner              | ShakeNDry           | Traffic             | Average             |
|---------------------|-------------|----------------|---------------------|---------------------|---------------------|---------------------|---------------------|---------------------|---------------------|
| GAP-TV [38]         | -           | -              | 33.08, 0.964        | 29.70, 0.914        | 29.48, 0.887        | 29.10, 0.878        | 29.59, 0.893        | 19.84, 0.645        | 28.47, 0.864        |
| DeSCI [15]          | -           | -              | 34.66, 0.971        | 32.88, 0.952        | 34.14, 0.938        | 36.16, 0.949        | 30.94, 0.905        | 24.62, 0.839        | 32.23, 0.926        |
| PnP-FFDNet [40]     | -           | -              | 34.15, 0.967        | 33.06, 0.957        | 34.80, 0.943        | 35.32, 0.940        | 32.37, 0.940        | 24.55, 0.837        | 32.38, 0.931        |
| PnP-FastDVDnet [41] | -           | -              | 35.27, 0.972        | 37.24, 0.971        | 35.63, 0.950        | 38.22, 0.965        | 33.71, 0.949        | 27.49, 0.915        | 34.60, 0.953        |
| BIRNAT [8]          | <b>4.14</b> | <b>1454.96</b> | 36.08, 0.975        | 38.30, 0.982        | 36.51, 0.956        | 39.65, 0.973        | 34.26, 0.951        | 28.03, 0.915        | 35.47, 0.959        |
| STFormer [26]       | 19.49       | 12155.47       | 37.37, <b>0.981</b> | 40.39, 0.988        | 38.32, 0.968        | 42.45, 0.985        | 35.15, 0.956        | 30.24, 0.939        | 37.32, 0.970        |
| EfficientSCI [25]   | 8.82        | 5701.50        | 37.51, 0.979        | 40.89, 0.988        | 38.49, 0.969        | 42.73, 0.985        | 35.19, 0.953        | 30.13, 0.943        | 37.49, 0.970        |
| EfficientSCI++ [6]  | 8.08        | <u>4256.20</u> | 37.53, 0.980        | 40.96, 0.989        | 38.50, 0.969        | 42.75, 0.985        | 35.18, 0.953        | 30.09, 0.942        | 37.50, 0.970        |
| DADUN [37]          | 10.44       | 20411.11       | 37.48, <b>0.981</b> | 41.49, <b>0.990</b> | <b>39.37, 0.973</b> | <u>43.34, 0.986</u> | 35.32, 0.957        | 30.31, 0.940        | 37.89, 0.972        |
| HiSViT [28]         | 8.98        | 6143.68        | <u>37.75, 0.981</u> | <u>41.50, 0.990</u> | <u>39.29, 0.972</u> | <u>43.27, 0.986</u> | <u>35.49, 0.958</u> | <u>30.79, 0.946</u> | <u>38.01, 0.972</u> |
| DU-9stg (Ours)      | <u>6.36</u> | 6298.62        | <b>37.92, 0.981</b> | <b>41.76, 0.990</b> | 39.28, <u>0.972</u> | <b>43.59, 0.987</b> | <b>35.73, 0.960</b> | <b>31.53, 0.952</b> | <b>38.30, 0.974</b> |

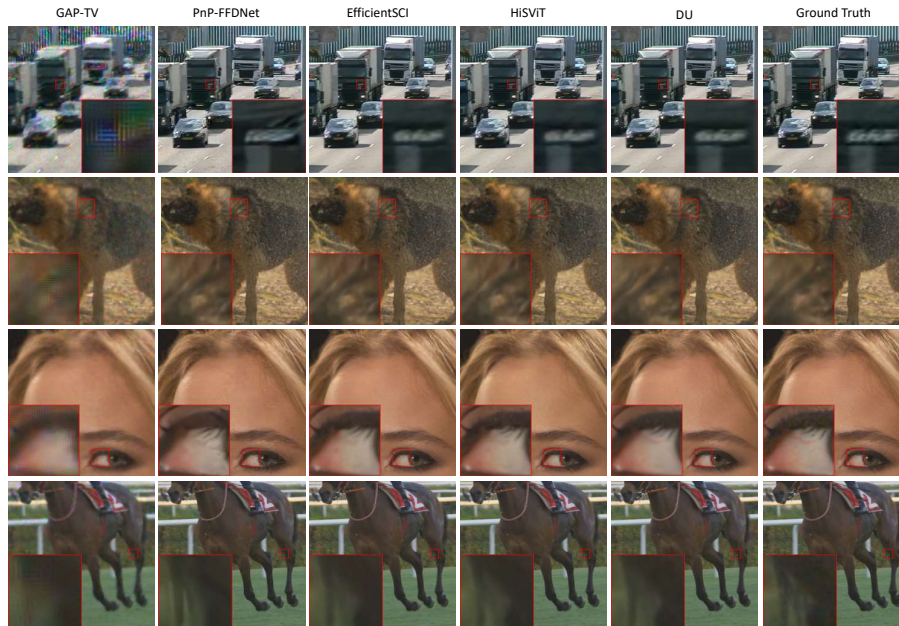


**Fig. 6:** Visual results of competitive methods on color video frames.

#### 4.4 Results on Real Captured Video

Due to the presence of more noise in real captured videos, the reconstruction task becomes more challenging. We provide the results of DU compared with GAP-TV [38], BIRNAT [8], PnP-FFDNet [40], STFormer [26], and HiSViT [28] on real datasets. Fig. 7 shows the visual reconstruction results of GAP-TV, PnP-FFDNet, STFormer, HiSViT, and our DU. We magnify local regions to obtain a clearer comparison. Our method can reconstruct sharper textures and detailed features. Specifically, it achieves the clearest reconstruction of the letters on the dominoes and WaterBallon.

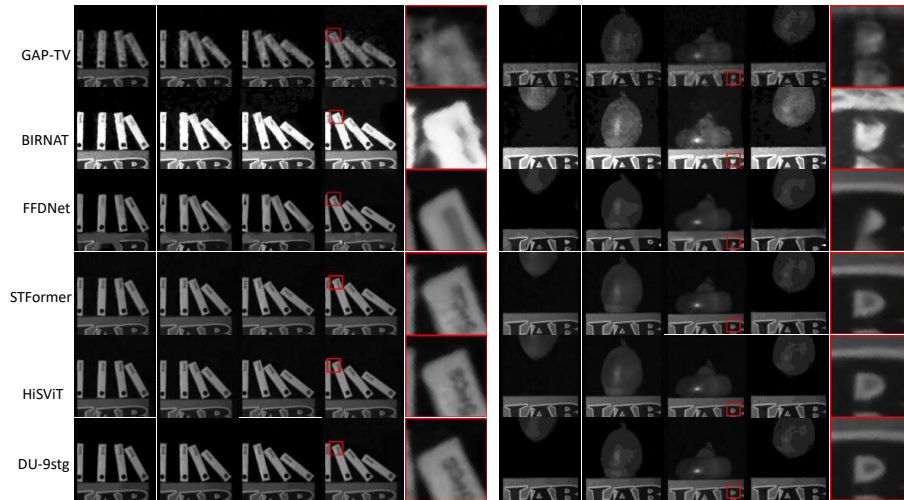


Fig. 7: Reconstructed results of real captured Duonimo and WaterBallon.

Table 3: Impact of the different periodicity.

| Periodicity    | Stage | Params | FLOPs   | PSNR  | SSIM   |
|----------------|-------|--------|---------|-------|--------|
| Baseline (T=1) | 5     | 7.66   | 1124.58 | 33.43 | 0.9512 |
| T=2            | 5     | 5.27   | 982.24  | 33.38 | 0.9515 |
| T=4            | 5     | 3.95   | 899.64  | 33.37 | 0.9502 |
| Baseline (T=1) | 9     | 13.79  | 2024.24 | 33.93 | 0.9557 |
| T=2            | 9     | 8.83   | 1724.33 | 33.99 | 0.9565 |
| T=4            | 9     | 6.36   | 1574.37 | 33.96 | 0.9563 |
| T=8            | 9     | 5.12   | 1499.39 | 33.69 | 0.9539 |

Table 4: Effect of DRP on other unfolding methods. \* means that we apply the DRP to the corresponding method, with the periodicity set to 4.

| Method      | Params | FLOPs   | PSNR  | SSIM   |
|-------------|--------|---------|-------|--------|
| DUN-3DUnet  | 61.91  | 3975.83 | 30.75 | 0.9188 |
| DUN-3DUnet* | 15.82  | 1261.58 | 30.91 | 0.9193 |
| DADUN       | 7.11   | 3356.21 | 33.28 | 0.9495 |
| DADUN*      | 4.04   | 1751.32 | 33.58 | 0.9522 |

#### 4.5 Ablation Study

To evaluate the contribution of each component in the DU framework, as well as the impact of different periodicity designs of DEF and the influence of DRP on other unfolding methods, we performed ablation experiments on grayscale videos.

**Impact of the differential periodicity.** To investigate the impact of different periodicities  $T$  on the reconstruction results, we set the model without a differential evolutionary stage (i.e.,  $T = 1$ ) as Baseline, and conduct ablation experiments on models with 5 and 9 stages for various values of  $T$ . As shown in the Tab. 3, when  $T = 4$ , the model achieves a favorable balance between performance and parameter efficiency.

**DRP for other unfolding methods.** To evaluate the effectiveness of DRP in other unfolding methods, we applied DRP to DUN-3DUnet and DADUN for ablation experiments, with the periodicity set to 4. As shown in the Tab. 4, applying

**Table 5:** Comparison of DRA and **Table 6:** Comparison of DM-FFN and competitive FFN

| Method        | Params | FLOPs  | PSNR  | SSIM   |
|---------------|--------|--------|-------|--------|
| Baseline-2    | 3.77   | 809.08 | 32.88 | 0.9463 |
| BDA [42]      | 3.89   | 872.80 | 33.00 | 0.9466 |
| SLTW-MSA [26] | 3.89   | 872.73 | 33.15 | 0.9484 |
| CSS-MSA [28]  | 3.90   | 872.64 | 33.22 | 0.9495 |
| DRA           | 3.95   | 899.64 | 33.37 | 0.9502 |

| Method       | Params | FLOPs   | PSNR  | SSIM   |
|--------------|--------|---------|-------|--------|
| Baseline-3   | 3.60   | 723.02  | 32.85 | 0.9461 |
| Regular FFN  | 3.87   | 862.52  | 32.98 | 0.9465 |
| GRFFN [26]   | 4.32   | 1088.64 | 32.57 | 0.9455 |
| GSM-FFN [28] | 4.24   | 1048.14 | 33.27 | 0.9497 |
| DM-FFN       | 3.95   | 899.64  | 33.37 | 0.9502 |

DRP to the aforementioned unfolding methods substantially reduces both computational cost and parameter count, while also improving performance, demonstrating that our DRP can be broadly applied to other unfolding frameworks to achieve superior results.

**Attention Comparison.** To study the effect of our DRA, we perform ablation with other attention designs. Baseline-2 is obtained by removing DRA from DU-5stg. G-MSA [11] and F-MSA [1] are impractical because their computational complexities scale quadratically with the spatial-temporal resolution  $T \times H \times W$  and the spatial resolution  $H \times W$ , respectively. BDA [42] computes spatiotemporal correlations simultaneously within a 3D window. SLTW-MSA [26] adopts a space-time factorization mechanism and computes spatial-window attention and temporal attention separately. CSS-MSA [28] attends to all spatial-temporal tokens with cross-scale interactions in a single attention layer. As shown in Tab. 5, baseline-2 yields 32.88 dB. Our DRA yields the most significant improvement higher than other attentions.

**Feed-Forward Network Comparison.** To study the effect of our DM-FFN, we perform ablation with other FFN designs. Baseline-3 is obtained by removing DM-FFN from DU-5stg. GR-FFN [26] conducts more feature mapping by grouping and using the residual mechanism to achieve multi-layer information fusion. GSM-FFN [28] strengthens the locality by introducing gated self-modulation to regular FFN. DM-FFN [28] strengthens the locality by introducing gated self-modulation to regular FFN. As shown in Tab. 6, baseline-3 yields 32.85 dB. Our DM-FFN yields the most improvement higher than regular FFN, GR-FFN and GSM-FFN.

## 5 Conclusion

We presented Differential Unfolding (DU) to address inefficiencies in conventional deep unfolding networks for video SCI. By leveraging a Differential Evolutionary Framework, DU combines high-fidelity general stages with lightweight differential stages, using DRP to model cross-stage feature evolution efficiently. This stage-wise focus on dynamic updates significantly improves reconstruction accuracy while reducing computational cost, establishing new state-of-the-art performance.

## References

1. Arnab, A., Dehghani, M., Heigold, G., Sun, C., Lučić, M., Schmid, C.: Vivit: A video vision transformer. In: 2021 IEEE/CVF International Conference on Computer Vision (ICCV). pp. 6816–6826 (2021). <https://doi.org/10.1109/ICCV48922.2021.00676>
2. Bertasius, G., Wang, H., Torresani, L.: Is space-time attention all you need for video understanding? In: Meila, M., Zhang, T. (eds.) Proceedings of the 38th International Conference on Machine Learning. Proceedings of Machine Learning Research, vol. 139, pp. 813–824. PMLR (18–24 Jul 2021)
3. Cai, Y., Lin, J., Wang, H., Yuan, X., Ding, H., Zhang, Y., Timofte, R., Gool, L.V.: Degradation-aware unfolding half-shuffle transformer for spectral compressive imaging. In: Koyejo, S., Mohamed, S., Agarwal, A., Belgrave, D., Cho, K., Oh, A. (eds.) Advances in Neural Information Processing Systems. vol. 35, pp. 37749–37761. Curran Associates, Inc. (2022)
4. Cao, M., Wang, L., Wang, H., Wang, G., Yuan, X.: Towards real-time video compressive sensing on mobile devices. In: Proceedings of the 32nd ACM International Conference on Multimedia. p. 11080–11088. MM '24, Association for Computing Machinery, New York, NY, USA (2024). <https://doi.org/10.1145/3664647.3680561>
5. Cao, M., Wang, L., Wang, H., Yuan, X.: A simple low-bit quantization framework for Å video snapshot compressive imaging. In: Leonardis, A., Ricci, E., Roth, S., Russakovsky, O., Sattler, T., Varol, G. (eds.) Computer Vision – ECCV 2024. pp. 112–129. Springer Nature Switzerland, Cham (2025)
6. Cao, M., Wang, L., Zhu, M., Yuan, X.: Hybrid cnn-transformer architecture for efficient large-scale video snapshot compressive imaging. International Journal of Computer Vision pp. 1–20 (2024)
7. Cheng, Z., Chen, B., Liu, G., Zhang, H., Lu, R., Wang, Z., Yuan, X.: Memory-efficient network for large-scale video compressive sensing. 2021 IEEE/CVF Conference on Computer Vision and Pattern Recognition (CVPR) pp. 16241–16250 (2021)
8. Cheng, Z., Chen, B., Lu, R., Wang, Z., Zhang, H., Meng, Z., Yuan, X.: Recurrent neural networks for snapshot compressive imaging. IEEE Transactions on Pattern Analysis and Machine Intelligence **45**(2), 2264–2281 (2023). <https://doi.org/10.1109/TPAMI.2022.3161934>
9. Chu, X., Tian, Z., Zhang, B., Wang, X., Shen, C.: Conditional positional encodings for vision transformers. In: International Conference on Learning Representations (2021)
10. Donoho, D.: Compressed sensing. IEEE Transactions on Information Theory **52**(4), 1289–1306 (2006). <https://doi.org/10.1109/TIT.2006.871582>
11. Dosovitskiy, A., Beyer, L., Kolesnikov, A., Weissenborn, D., Zhai, X., Unterthiner, T., Dehghani, M., Minderer, M., Heigold, G., Gelly, S., Uszkoreit, J., Houshy, N.: An image is worth 16x16 words: Transformers for image recognition at scale. ICLR (2021)
12. Gao, L., Liang, J., Li, C., Wang, L.V.: Single-shot compressed ultrafast photography at one hundred billion frames per second. Nature **516**(7529), 74–77 (Dec 2014). <https://doi.org/10.1038/nature14005>
13. Hitomi, Y., Gu, J., Gupta, M., Mitsunaga, T., Nayar, S.K.: Video from a single coded exposure photograph using a learned over-complete dictionary. In: 2011 International Conference on Computer Vision. pp. 287–294 (2011). <https://doi.org/10.1109/ICCV.2011.6126254>

14. Kingma, D.P., Ba, J.: Adam: A method for stochastic optimization. *CoRR abs/1412.6980* (2014)
15. Liu, Y., Yuan, X., Suo, J., Brady, D.J., Dai, Q.: Rank minimization for snapshot compressive imaging. *IEEE Transactions on Pattern Analysis and Machine Intelligence* **41**(12), 2990–3006 (2019). <https://doi.org/10.1109/TPAMI.2018.2873587>
16. Llull, P., Liao, X., Yuan, X., Yang, J., Kittle, D., Carin, L., Sapiro, G., Brady, D.J.: Coded aperture compressive temporal imaging. *Optics Express* **21**(9), 10526 (Apr 2013). <https://doi.org/10.1364/oe.21.010526>
17. Loshchilov, I., Hutter, F.: Sgdr: Stochastic gradient descent with warm restarts. *arXiv: Learning* (2016)
18. Lu, R., Cheng, Z., Chen, B., Yuan, X.: Motion-aware dynamic graph neural network for video compressive sensing. *IEEE Transactions on Pattern Analysis and Machine Intelligence* **46**(12), 7850–7866 (2024). <https://doi.org/10.1109/TPAMI.2024.3395804>
19. Ma, J., Liu, X.Y., Shou, Z., Yuan, X.: Deep tensor admm-net for snapshot compressive imaging. In: 2019 IEEE/CVF International Conference on Computer Vision (ICCV). pp. 10222–10231 (2019). <https://doi.org/10.1109/ICCV.2019.01032>
20. Meng, Z., Yuan, X., Jalali, S.: Deep Unfolding for Snapshot Compressive Imaging. *International Journal of Computer Vision* **131**(11), 2933–2958 (Nov 2023). <https://doi.org/10.1007/s11263-023-01844-4>
21. Pont-Tuset, J., Perazzi, F., Caelles, S., Arbeláez, P., Sorkine-Hornung, A., Gool, L.V.: The 2017 davis challenge on video object segmentation. *ArXiv abs/1704.00675* (2017)
22. Qiao, M., Meng, Z., Ma, J., Yuan, X.: Deep learning for video compressive sensing. *APL Photonics* **5**(3), 030801 (Mar 2020). <https://doi.org/10.1063/1.5140721>
23. Reddy, D., Veeraraghavan, A., Chellappa, R.: P2c2: Programmable pixel compressive camera for high speed imaging. In: *CVPR 2011*. pp. 329–336 (2011). <https://doi.org/10.1109/CVPR.2011.5995542>
24. Sun, Y., Yuan, X., Pang, S.: Compressive high-speed stereo imaging. *Opt. Express* **25**(15), 18182–18190 (Jul 2017). <https://doi.org/10.1364/OE.25.018182>
25. Wang, L., Cao, M., Yuan, X.: Efficientsci: Densely connected network with space-time factorization for large-scale video snapshot compressive imaging. In: 2023 IEEE/CVF Conference on Computer Vision and Pattern Recognition (CVPR). pp. 18477–18486 (2023). <https://doi.org/10.1109/CVPR52729.2023.01772>
26. Wang, L., Cao, M., Zhong, Y., Yuan, X.: Spatial-temporal transformer for video snapshot compressive imaging. *IEEE Transactions on Pattern Analysis and Machine Intelligence* **45**(7), 9072–9089 (2023). <https://doi.org/10.1109/TPAMI.2022.3225382>
27. Wang, P., Wang, L., Yuan, X.: Deep optics for video snapshot compressive imaging. In: 2023 IEEE/CVF International Conference on Computer Vision (ICCV). pp. 10612–10622 (2023). <https://doi.org/10.1109/ICCV51070.2023.00977>
28. Wang, P., Zhang, Y., Wang, L., Yuan, X.: Hierarchical separable video transformer for snapshot compressive imaging. In: Leonardis, A., Ricci, E., Roth, S., Russakovsky, O., Sattler, T., Varol, G. (eds.) *Computer Vision – ECCV 2024*. pp. 104–122. Springer Nature Switzerland, Cham (2025)
29. Wang, Z., Zhang, H., Cheng, Z., Chen, B., Yuan, X.: Metasci: Scalable and adaptive reconstruction for video compressive sensing. 2021 IEEE/CVF Conference on Computer Vision and Pattern Recognition (CVPR) pp. 2083–2092 (2021)
30. Wang, Z., Bovik, A., Sheikh, H., Simoncelli, E.: Image quality assessment: from error visibility to structural similarity. *IEEE Transactions on Image Processing* **13**(4), 600–612 (2004). <https://doi.org/10.1109/TIP.2003.819861>

31. Wt, Z., Zhangt, J., Mou, C.: Dense deep unfolding network with 3d-cnn prior for snapshot compressive imaging. In: 2021 IEEE/CVF International Conference on Computer Vision (ICCV). pp. 4872–4881 (2021). <https://doi.org/10.1109/ICCV48922.2021.00485>
32. Wu, Z., Zhang, Z., Song, J., Zhang, M.: Spatial-temporal synergic prior driven unfolding network for snapshot compressive imaging. In: 2021 IEEE International Conference on Multimedia and Expo (ICME). pp. 1–6 (2021). <https://doi.org/10.1109/ICME51207.2021.9428320>
33. Xie, S., Huang, Y., Qu, G., Ge, Y.: Sampling-priors-augmented deep unfolding network for robust video compressive sensing. *Journal of the Franklin Institute* **362**(3), 107545 (2025). <https://doi.org/https://doi.org/10.1016/j.jfranklin.2025.107545>
34. Yang, C., Zhang, S., Yuan, X.: Ensemble learning priors unfolding for scalable Snapshot Compressive Sensing. arXiv e-prints arXiv:2201.10419 (Jan 2022). <https://doi.org/10.48550/arXiv.2201.10419>
35. Yang, J., Liao, X., Yuan, X., Llull, P., Brady, D.J., Sapiro, G., Carin, L.: Compressive sensing by learning a gaussian mixture model from measurements. *IEEE Transactions on Image Processing* **24**(1), 106–119 (2015). <https://doi.org/10.1109/TIP.2014.2365720>
36. Yang, J., Yuan, X., Liao, X., Llull, P., Brady, D.J., Sapiro, G., Carin, L.: Video compressive sensing using gaussian mixture models. *IEEE Transactions on Image Processing* **23**(11), 4863–4878 (2014). <https://doi.org/10.1109/TIP.2014.2344294>
37. Yin, J., Wang, N., Hu, B., Wang, Y., Wang, Q.: Degradation-aware deep unfolding network with transformer prior for video compressive imaging. *Signal Processing* **227**, 109660 (2025). <https://doi.org/https://doi.org/10.1016/j.sigpro.2024.109660>
38. Yuan, X.: Generalized alternating projection based total variation minimization for compressive sensing. In: 2016 IEEE International Conference on Image Processing (ICIP). pp. 2539–2543 (2016). <https://doi.org/10.1109/ICIP.2016.7532817>
39. Yuan, X., Brady, D.J., Katsaggelos, A.K.: Snapshot compressive imaging: Theory, algorithms, and applications. *IEEE Signal Processing Magazine* **38**(2), 65–88 (2021). <https://doi.org/10.1109/MSP.2020.3023869>
40. Yuan, X., Liu, Y., Suo, J., Dai, Q.: Plug-and-play algorithms for large-scale snapshot compressive imaging. In: 2020 IEEE/CVF Conference on Computer Vision and Pattern Recognition (CVPR). pp. 1444–1454 (2020). <https://doi.org/10.1109/CVPR42600.2020.00152>
41. Yuan, X., Liu, Y., Suo, J., Durand, F., Dai, Q.: Plug-and-play algorithms for video snapshot compressive imaging. *IEEE Transactions on Pattern Analysis and Machine Intelligence* **44**(10), 7093–7111 (2022). <https://doi.org/10.1109/TPAMI.2021.3099035>
42. Zheng, S., Yuan, X.: Unfolding framework with prior of convolution-transformer mixture and uncertainty estimation for video snapshot compressive imaging. In: 2023 IEEE/CVF International Conference on Computer Vision (ICCV). pp. 12692–12703 (2023). <https://doi.org/10.1109/ICCV51070.2023.01170>